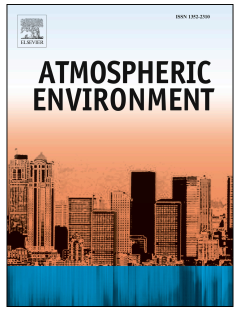

Horizontal flux of ozone in the planetary boundary layer in Hong Kong using wind LiDAR measurements

Changqing Lin, Jimmy C.H. Fung, Chao Ren, Edward Y.Y. Ng, Yuguo Li, Yueyang He, Kenneth K.M. Leung, Zhi Ning, Alexis K.H. Lau

PII: S1352-2310(23)00472-7

DOI: https://doi.org/10.1016/j.atmosenv.2023.120046

Reference: AEA 120046

To appear in: *Atmospheric Environment*

Received Date: 28 June 2023

Revised Date: 12 August 2023

Accepted Date: 18 August 2023

Contributors

Supervision: AKH Lau.

Analysis and draft: CQ Lin.

Conceptualization: CQ Lin.

Data: C Ren, EYY Ng, YG Li

Review and editing: JCH Fung, YY He, KKM Leung, Z Ning.

Horizontal flux of ozone in the planetary boundary layer in Hong Kong using wind LiDAR measurements

Changqing Lin,[1] Jimmy C.H. Fung,[1,2] Chao Ren,[3] Edward Y.Y. Ng,[4] Yuguo Li,[5] Yueyang He,[4] Kenneth K.M. Leung,[6] Zhi Ning,[1] Alexis K.H. Lau,[1,7,*]

[1]Division of Environment and Sustainability, The Hong Kong University of Science and Technology, Hong Kong, China

[2]Department of Mathematics, The Hong Kong University of Science and Technology, Hong Kong, China

[3]Faculty of Architecture, The University of Hong Kong, Hong Kong, China

[4]School of Architecture, The Chinese University of Hong Kong, Hong Kong, China

[5]Department of Mechanical Engineering, The University of Hong Kong, Hong Kong, China

[6]Air Policy Division, Environment and Ecology Bureau, Hong Kong Government SAR, Hong Kong, China

[7]Department of Civil and Environmental Engineering, The Hong Kong University of Science and Technology, Hong Kong, China

Corresponding author: alau@ust.hk

Abstract. While the crucial roles of ozone (O_3) transport in the planetary boundary layer (PBL) have been acknowledged for some time, there is currently limited knowledge about this aspect primarily due to the limited availability of measurements to determine the characteristics of the PBL. In this study, measurements from a wind Light Detection and Ranging (LiDAR) system were taken to monitor vertical profile of wind pattern at an urban site in Hong Kong in September 2022, a period when the city was frequently impacted by tropical cyclones and experienced severe O_3 pollution levels. The PBL height was identified based on the vertical profile of wind speed shear. By combining information on the PBL height, vertical wind profile, and O_3 concentration, we performed a cross-sectional analysis to explore the total horizontal flux (THF) of O_3 across the PBL in Hong Kong. Throughout the entire study month, the THF of O_3 exhibited a predominant easterly component. However, during the O_3 pollution episodes, the THF of O_3 exhibited a predominant westerly component, indicating an increased regional transport from Greater Bay Area (GBA). The westerly winds between 240° and 300° contributed 61.2% to the total flux of O_3 in the PBL during these episodes. In addition, clockwise veering winds were observed from the ground to the top of the PBL, which can be attributed to the Ekman spiral. As a result, during the O_3 pollution episodes, the wind with the peak O_3 flux shifted from westerly to northwesterly as the height increased in the PBL. The northwesterly THF of O_3 between 290° and 300° reached its peak at 600 m above ground level during these episodes. These findings enhance our understanding of the 3D pollutant transports for both long-term averages and short-term pollution episodes in the GBA and Hong Kong.

Keywords: LiDAR, Ozone, Pollution flux, Planetary boundary layer, Vertical variation.

1. Introduction

The Greater Bay Area (GBA) has become one of the largest city clusters in the world due to rapid urbanization and industrialization (Yu et al., 2023). However, in exchange for its tremendous economic development, the region has also experienced high levels of air pollution (Fan and Li, 2023). In recent years, ozone (O_3) pollution has become prominent due to the non-linear response of O_3 to the emission controls of its precursors (Guo et al., 2023; Tang et al., 2022). Because O_3 is a secondary pollutant, regional transport can play a dominant role in the formation of severe O_3 pollution episodes in the GBA region (Li et al., 2013; Shen et al., 2022). Although various efforts have been made to identify the causes of severe O_3 pollution episodes, a complete picture of the three-dimensional (3D) transport of O_3 in this region remains unclear due to a lack of upper-air observations.

The regional transport of O_3 is largely determined by the 3D wind field in the planetary boundary layer (PBL), which, however, is highly variable (Zhang et al., 2023). The wind field in the PBL over the GBA region can be influenced by various factors, such as synoptic weather patterns, mesoscale atmospheric circulations, urban heat island effect, and complex terrain (He et al., 2021; Xia et al., 2023). For instance, confluence zones of wind fields are often found at different locations in Hong Kong due to atmospheric circulations (Fung et al., 2005). Yang et al. (2019) analyzed severe air pollution in Hong Kong and found that strong vertical wind shear within the PBL was positively correlated with surface pollutant concentrations during pollution episodes. Therefore, the characteristics of the wind field in the PBL can significantly influence the development of severe air pollution episodes (Cruz et al., 2023; Yan et al., 2022).

It is common to observe winds veering from the bottom to the top of the PBL, which is denoted as the Ekman spiral (Ekman and Kullenberg, 1905). This can be attributed to the decrease in friction as a significant force with increasing height. The winds are geostrophic in the free atmosphere, resulting from a balance between the pressure gradient force and Coriolis effect. As a consequence, wind direction is parallel to the isobars. However, within the PBL, the pressure gradient force and Coriolis effect are augmented by the frictional force. Friction causes air to spiral into low pressure areas since it reduces the magnitude of the Coriolis force. Theoretically, the wind direction in the PBL rotates clockwise with altitude in the northern hemisphere. This phenomenon was reported in Beijing using a radar wind profiler (Wang et al., 2023). A similar spiral-shaped wind profile was observed in another study in Beijing using measurements from a meteorological tower (Zhang et al., 2021). Due to the opposite Coriolis effect in the southern hemisphere, the wind direction may rotate counterclockwise with altitude in the PBL (Potts et al., 2023). Considering the veering wind profiles, which may impose significant asymmetrical loadings on structures, becomes essential in the design of super-tall buildings or gigantic wind turbines (Tse et al., 2016). However, observational investigation of the impacts of the wind spiral on pollution transport remains limited.

In addition to the wind field in the PBL, the height of the PBL also plays an important role in governing the evolution of severe air pollution episodes (Paul and Das, 2022). Pollutants released from the ground are often trapped within the PBL (Jiang et al., 2022). This is because the PBL is characterized by a capping inversion layer at its top (Liu et al., 2022). As a result, the interactions of mass and momentum between the PBL and free atmosphere are limited. In specific meteorological conditions, the suppressed PBL can contribute significantly to the rapid increase in ground-level pollutant concentrations (Su et al., 2020). Thus, the majority of pollutant transport between different regions occurs within the PBL. Quantifying this transport within the PBL is crucial for understanding the regional transport of air pollutants.

While the crucial roles of O_3 transport in the PBL have been acknowledged for some time, there is currently limited knowledge about this aspect. This is primarily attributed to the limited availability of measurements to determine the characteristics of the PBL. Previous studies were mostly conducted based on ground-level measurements, which are insufficient to depict a complete picture of 3D wind and pollution fields. Vertical measurements have mainly relied on aircraft, meteorological tower, and balloon-borne monitoring (Zhou et al., 2022). These vertical measurements, however, either lack spatiotemporal resolution or are costly in terms of data collection (Li et al., 2022). The detailed variations in the wind field and pollutant transport in the PBL have yet to be fully understood. To overcome these limitations, a monitoring system capable of continuously collecting data throughout the PBL is necessary.

Recent developments in Light Detection and Ranging (LiDAR) technology have enabled accurate remote sensing of the vertical structure of PBL at a high spatiotemporal resolution, representing a substantial improvement over traditional ground-level measurements (Chen et al., 2023). By detecting the Doppler shift of laser signals, wind LiDAR can detect vertical distribution of wind speed and direction (Yang et al., 2022). In recent years, there has been a growing adoption of LiDAR technologies in air quality studies. For instance, Wang et al. (2019) applied a wind LiDAR system to monitor the vertical variation in wind velocity and the evolution of the urban boundary layer during a pollution episode in Beijing. Similarly, Park et al. (2022) employed wind LiDAR measurements to investigate the variations in the PBL height at an urban site in Seoul, Korea.

In this study, measurements from a wind Light Detection and Ranging (LiDAR) system were taken to monitor vertical profile of wind pattern at an urban site in Hong Kong in September 2022, a period when the city was frequently impacted by tropical cyclones and experienced severe

O_3 pollution levels. The PBL height was identified using the vertical profile of wind shear. By combining information on the PBL height, vertical wind profile, and O_3 concentration, we explored the horizontal flux of O_3 across the PBL in Hong Kong. The vertical variation in the O_3 flux was evaluated. The dependence of the horizontal flux of O_3 on the wind direction during the entire study period and the pollution episodes was analyzed. Cross-sectional analyses of the O_3 flux can help to provide answers to questions such as how many pollutants were transported from the central GBA into Hong Kong. Overall, this study aims to enhance our understanding of the 3D pollutant transports for both long-term averages and short-term pollution episodes in the GBA and Hong Kong.

2. Data and methodology

2.1 Wind LiDAR measurements

The wind LiDAR system, model WINDCUBE 100S, was produced by Leosphere, a Vaisala company. As shown in Figure S1, it was located at the Hong Kong Observatory (HKO) situated at King's Park in Hong Kong (22.3132°N, 114.1704°E), and operated in the Doppler Beam Swinging (DBS) mode. This mode detects the Doppler shifts of infrared laser signals that are backscattered by aerosols in the atmosphere. Measurements of hourly horizontal wind speed (W) and direction (θ) were taken from 50 m to 3.1 km above ground level (AGL), with a vertical resolution of 25 m. For further information on the algorithm used and the uncertainty of the wind LiDAR measurements, please refer to He et al. (2021). As shown in Figure S2, the quantity of valid samples decreases as the height increases, owing to the presence of clouds and the lack of aerosols in the free atmosphere. Nevertheless, the majority of wind data, specifically below 1 km, remains available.

2.2 Meteorological and O_3 data

To assess the accuracy of the wind LiDAR measurements during the study period, ground-level and upper-level wind data were obtained from collocated sources. Hourly ground-level wind data were obtained from the Automatic Weather Station (AWS) at King's Park, while upper-level wind data were collected through radiosonde measurements conducted at King's Park. The radiosonde measurements were available at 8:00 am and 20:00 pm (China's local time in UTC+8 was used in this study) throughout the study period. In addition, hourly data on O_3 concentrations at Sham Shui Po (22.3315°N, 114.1567°E), which is situated adjacent to King's Park, were used to explore the O_3 flux. To gain a better understanding of the vertical variation in O_3 concentration in the PBL, we obtained the O_3 data at Tai Mo Shan (22.4102°N, 114.1245°E), which is situated at an elevation of 950 meters above sea level.

2.3 PBL height

The height of PBL can be identified by analyzing various profiles, such as vertical velocity variance, wind speed shear, and wind directional shear (Tucker et al., 2009). As a result of surface friction, winds within the PBL are typically weaker than those in the free atmosphere. In the layer above the PBL, the wind speed becomes more uniform as the effect of friction decreases significantly. Large wind shear can be present at the top of the PBL (Canut et al., 2012; Lindvall and Svensson, 2019). Therefore, the PBL height can be defined as the altitude of a transition layer where there is a marked change in wind behavior.

The identification of the PBL height in this study is based on the vertical profile of wind speed shear. To be specific, the gradient of the horizontal wind speed is estimated as a function of height in order to determine the vertical distribution of wind speed shear (unit: s^{-1}):

$$\eta = \frac{W(z_{i+1}) - W(z_i)}{z_{i+1} - z_i} \qquad (1)$$

where z denotes the altitude (unit: m); $z_{i+1} - z_i$ represents the vertical resolution of the LiDAR measurement, which is 25 m; and W represents the horizontal wind speed (unit: m/s). Then, the PBL height can be determined by identifying the height at which the gradient of the horizontal wind speed reaches its maximum value with respect to altitude. It should be noted, however, that the wind shear can also be significant near the ground. For this reason, the wind data collected below 100 m near the ground were excluded from the PBL estimation process to ensure the accuracy of the results.

2.4 Horizontal flux of O_3

Horizontal flux of O_3 was analyzed based on the wind LiDAR measurements to gain insights into O_3 transport in the study region. The flux represents the mass flow per unit cross-sectional area per unit time (unit: g/(m^2·s)):

$$f = c \cdot W \tag{2}$$

where c denotes the O_3 concentration (unit: μg/m^3). The total horizontal flux (THF) of O_3 through a cross-sectional area of 1 m^2 during the study period at a given direction θ and altitude z can be estimated as follows (unit: g/m^2):

$$THF(\theta, z) = \sum_{t=1}^{N} f(\theta, z, t) \cdot \Delta t = \sum_{t=1}^{N} c(z, t) \cdot W(\theta, z, t) \cdot \Delta t \tag{3}$$

where θ is the direction; t represents time; and Δt (which is 1 hour) indicates the temporal resolution of LiDAR measurements. For the purposes of this study, it was assumed that O_3 within the PBL was well mixed. Consequently, the temporal variation in O_3 concentration was taken into account. The dependence of the THF of O_3 on both direction (θ) and altitude (z) was analyzed to improve our understanding of the 3D transport of O_3 over Hong Kong.

The analysis then proceeded to examine the THF of O_3 through the entire PBL (Figure 1). At a given direction θ, the THF of O_3 through a cross-sectional area with a width of 1 m across the entire PBL during the study period can be estimated as follows (unit: kg):

$$THF(\theta)_{PBL} = \sum_{t=1}^{N} \sum_{z=1}^{H(t)} c(z,t) \cdot W(\theta,z,t) \cdot \Delta z \cdot 1m \cdot \Delta t \quad (4)$$

where Δz (which is 25 m) represents the vertical resolution of LiDAR measurements. The dependence of the THF of O_3 across the entire PBL on direction (θ) was then analyzed to help understand the O_3 transport in the study region.

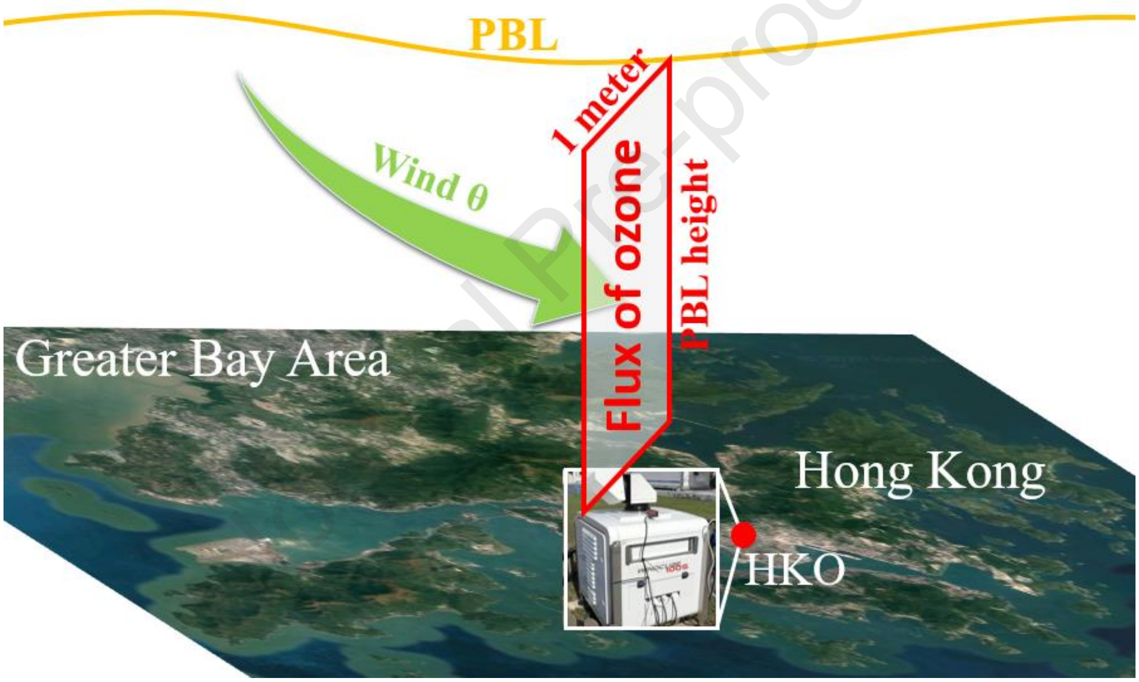

Figure 1. Experimental setup for estimating the total horizontal flux (THF) of O_3 through a cross-sectional area across the PBL in Hong Kong.

3. Results

3.1 O_3 variation

Time series of O_3 concentration at Sham Shui Po in September 2022 is presented in Figure S3. Based on the monthly average, the O_3 concentration is estimated to be 101.47 ± 51.98 μg/m^3. The grey line in the figure marks the threshold of 160 μg/m^3, which was used to identify O_3

pollution episodes in this study. During the study period, there were frequent O_3 pollution episodes, and the maximum concentration of over 300 μg/m^3 was recorded on September 13. The hourly O_3 concentration exceeded the threshold for 78 hours, which is equivalent to 10.8% of the study month.

3.2 Wind variation

Ground-level and upper-level wind data were used to assess the accuracy of the wind LiDAR measurements during the study period. Panel (a) of Figure 2 shows time series of wind speed and direction at 50 m AGL from LiDAR measurements and at 10 m AGL from ground-based AWS measurements in September 2022. The wind LiDAR measurements were found to be in good agreement with the ground-based measurements. The average wind speed at 10 m AGL was slightly lower than that at 50 m AGL. Based on monthly averages, the estimated wind speed at 10 m AGL and 50 m AGL at King's Park were 2.9 ± 1.3 m/s and 3.2 ± 1.4 m/s, respectively. Panel (b) shows the time series of wind speed and direction at 900 m AGL as measured by the wind LiDAR and radiosonde instruments. Once again, the results showed good agreement between the LiDAR and sounding measurements.

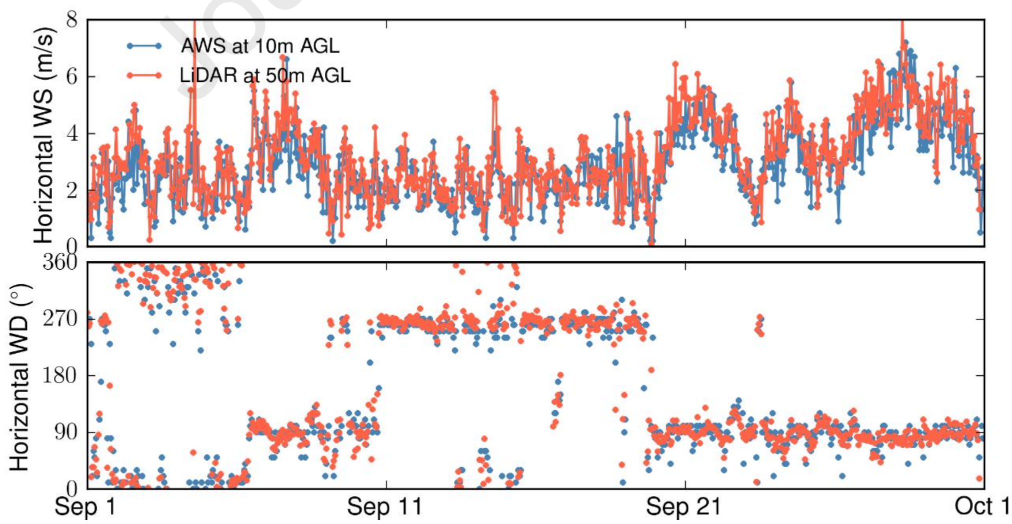

(a)

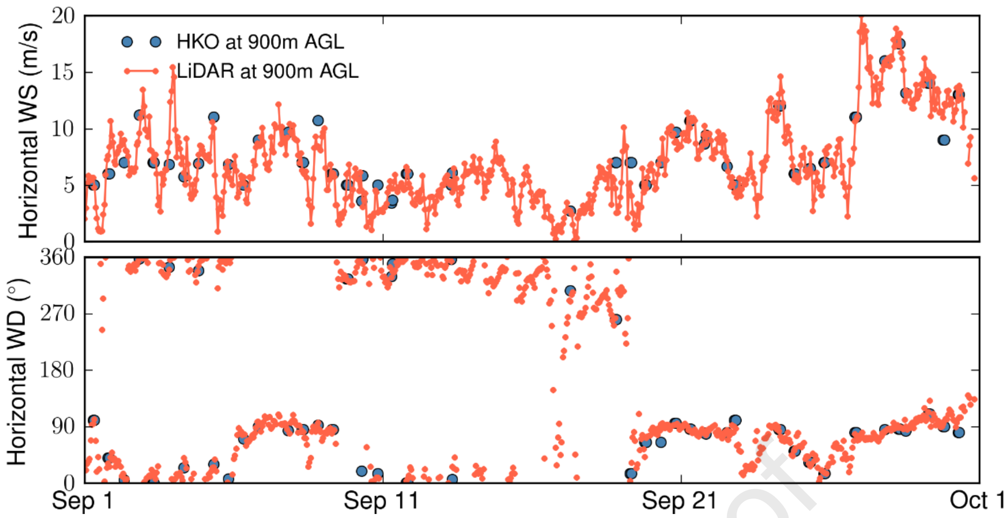

(b)

Figure 2. (a) Time series of wind speed and direction at 50 m AGL from LiDAR measurements and at 10 m AGL from ground-based AWS measurements in September 2022. (b) Time series of wind speed and direction at 900 m AGL obtained from LiDAR and radiosonde measurements in September 2022.

Since wind is a vector, two components were evaluated separately: the east-west (U) and north-south (V) wind speeds. Positive U and V wind speeds correspond to westerly and southerly winds, respectively, while negative U and V wind speeds correspond to easterly and northerly winds, respectively. Panels (a) and (b) of Figure S4 present a comparison of the U and V wind velocities at 50 m AGL as measured by the wind LiDAR and at 10 m AGL by the ground-based AWS monitoring at King's Park during the study month. The comparison revealed good agreement, with correlation coefficients of 0.94 and 0.71 (N = 698) for the U and V wind speeds, respectively. Panels (c) and (d) depict a comparison of the U and V wind speeds at 900 m AGL as measured by the wind LiDAR and radiosonde instruments at King's Park. The comparison showed good agreement, with correlation coefficients of 0.98 and 0.88 (N = 68) for the U and V wind speeds, respectively.

The time-series evaluations indicated that wind behavior varied with altitude. Figure 3 compares the wind roses at 50 m and 900 m AGL as measured by the wind LiDAR in September 2022. At 50 m AGL, the winds were mainly composed of easterly and westerly winds. As the altitude increased, the westerly components shifted to northerly and northwesterly. The clockwise veering winds from the bottom to the top of the PBL can be attributed to the Ekman spiral, resulting from the decrease in friction as a significant force with increasing height. The winds are geostrophic in the free atmosphere. As a consequence, wind direction is parallel to the isobars. When a tropical cyclone is located to the east of Hong Kong, the dominant wind in the free atmosphere becomes northerly. However, within the PBL, friction causes air to spiral into low pressure areas since it reduces the magnitude of the Coriolis force. Therefore, when the tropical cyclone is located to the east of Hong Kong, the dominant winds near the ground turn westerly or northwesterly.

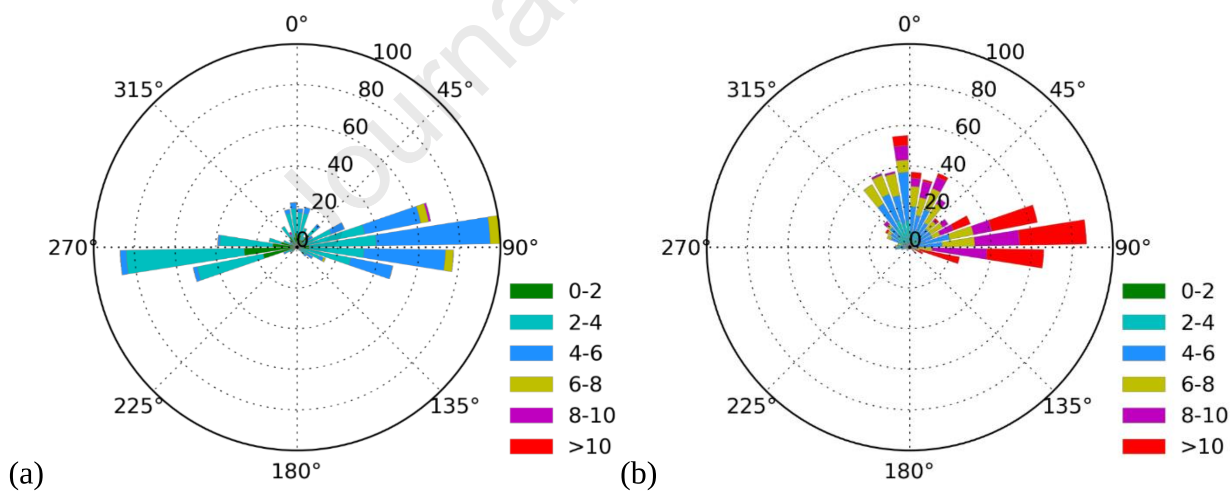

Figure 3. Wind roses at (a) 50 m and (b) 900 m AGL as measured by the wind LiDAR in September 2022.

3.3 PBL height

The vertical profile of wind speed shear was used to identify the PBL height. An example is provided in Figure S5. Panel (a) of it shows the vertical distribution of horizontal wind speed (W) at 20:00 pm on September 11, 2022. Due to surface friction, wind speeds within the PBL are usually lower than those in the free atmosphere. The corresponding vertical profile of the wind speed shear is presented in panel (b). The PBL height can be determined by identifying the height at which the gradient of the horizontal wind speed reaches its maximum value with respect to altitude. Based on this criterion, the PBL height was estimated to be 0.62 km.

Panel (a) of Figure 4 shows the time series of the PBL height, along with the vertical distribution of horizontal wind speed (W) from September 8 to 15, 2022. The corresponding vertical distributions of U and V wind speeds are displayed in panels (b) and (c), respectively. As depicted in Figure S6, the tropical cyclone "Muifa" moved towards the Asian continent and was situated near Taiwan on September 12. When Hong Kong was impacted by the air subsidence at the outer edge of the tropical cyclone, the atmosphere became more stable, and the PBL height dropped. As a result, the PBL height decreased from around 1 km on September 10 to approximately 200 m on September 14. The suppressed PBL can hinder the vertical dispersion of air pollutants. In addition, when the tropical cyclone affected Hong Kong, the dominant winds changed from easterly to westerly. These westerly winds transported air pollutants from the central GBA into Hong Kong, thereby contributing to a rapid increase in pollutant concentrations in Hong Kong. Moreover, strong northerly geostrophic winds were present above the PBL due to the balance between the pressure gradient force and Coriolis effect.

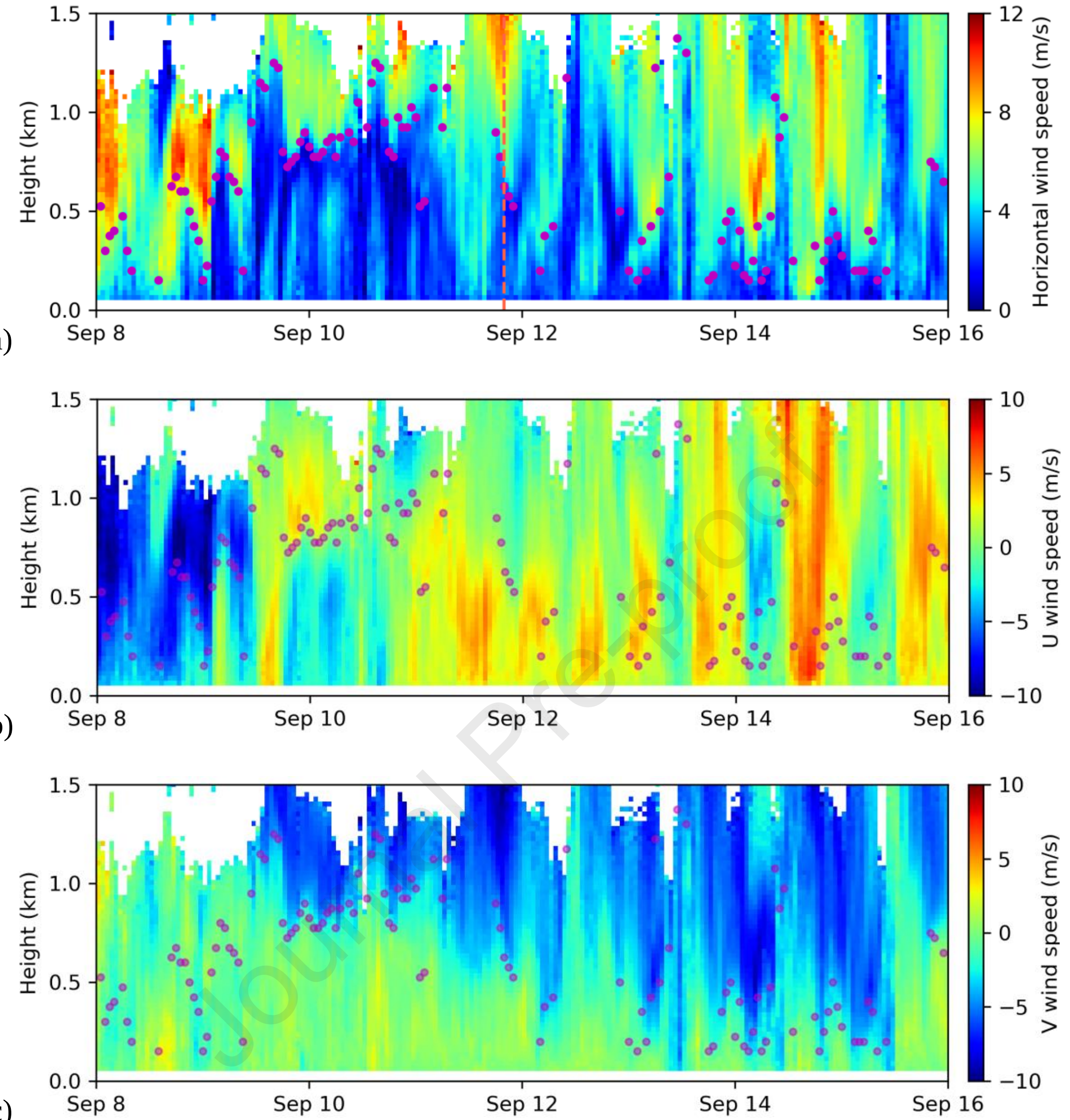

(a) (b) (c)

Figure 4. Time series of the PBL height (purple dots), along with the vertical distributions of (a) horizontal wind speed, (b) U wind speed, and (c) V wind speed from September 8 to 15, 2022. The red dashed line marks the example data used in Figure S5.

Based on the estimated PBL throughout the study month, Figure S7 shows the diurnal variation in the monthly average PBL height, along with the vertical distribution of horizontal wind speed in September 2022. During the study month, the average PBL height was 0.56 ± 0.34 km. A significant diurnal variation was found, with the PBL height increasing in the morning and reaching its peak at noontime and early afternoon (e.g., 0.74 ± 0.38 km at 12:00 pm). This diurnal pattern is attributable to the variation in solar heating throughout the day, which, in turn, affects the convection of the atmosphere.

3.4 Vertical variance in O_3 flux

By combining information on the PBL height, vertical wind profile, and O_3 concentration, we explored the vertical variance in the THF of O_3 across the PBL. Figure 5 shows the THF of O_3 through a unit cross-sectional area for various directions, with a resolution of 10°, at three altitudes during the entire month of September 2022. Throughout the study month, the THF of O_3 exhibited a predominant easterly component at all three altitudes. Table 1 summarizes the THF of O_3 through a unit cross-sectional area for six primary groups of directions: 0-60°, 60-120°, 120-180°, 180-240°, 240-300°, and 300-360°. The easterly winds between 60° and 120° contributed 50.8%, 52.3%, and 52.5% to the total flux of O_3 at 50 m, 300 m, and 500 m, respectively. The predominant easterly component of O_3 flux can be attributed to the dominant easterly wind pattern during the study month.

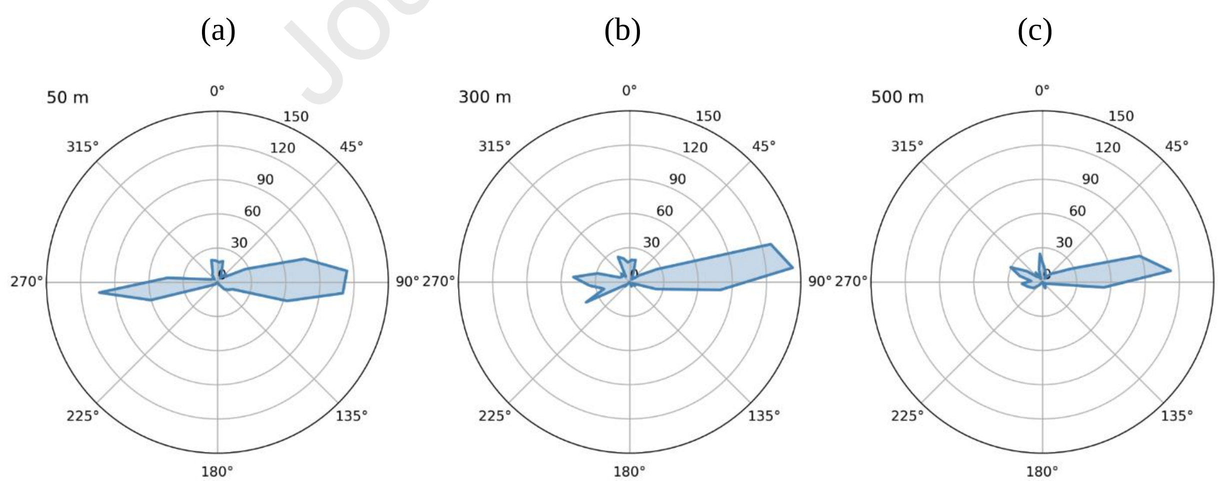

Figure 5. The THF of O_3 through a unit cross-sectional area for various directions at (a) 50 m, (b) 300 m, and (c) 500m AGL during the entire month of September 2022 (unit: g/m^2).

Table 1. The THF of O_3 through a unit cross-sectional area for six primary groups of directions at 50 m, 300 m, and 500 m AGL during the entire study month. The percentage contributions of each component are indicated in parentheses.

Altitudes	THF of O_3 through a unit cross-sectional area (unit: g/m^2)					
	0-60°	60-120°	120-180°	180-240°	240-300°	300-360°
50 m	67.93 (8.4%)	408.92 (50.8%)	23.32 (2.9%)	6.54 (0.8%)	231.75 (28.8%)	65.83 (8.2%)
300 m	63.26 (8.2%)	404.18 (52.3%)	18.05 (2.3%)	11.15 (1.4%)	188.66 (24.4%)	87.25 (11.3%)
500 m	59.20 (10.6%)	291.82 (52.5%)	13.90 (2.5%)	14.90 (2.7%)	104.28 (18.7%)	72.18 (13.0%)

Similar analyses were performed to investigate the horizontal flux of O_3 during the O_3 pollution episodes. Figure 6 shows the THF of O_3 through a unit cross-sectional area for various directions, with a resolution of 10°, at three altitudes during the O_3 pollution episodes in September 2022. During the O_3 pollution episodes, the THF of O_3 exhibited a predominant westerly component at all three altitudes. Table 2 summarizes the THF of O_3 through a unit cross-sectional area for six primary groups of directions. The westerly winds between 240° and 300° contributed 78.1%, 71.9%, and 64.7% to the total flux of O_3 at 50 m, 300 m, and 500 m, respectively. The predominant westerly component of O_3 flux can be attributed to the change in the dominant wind pattern when the tropical cyclone affected Hong Kong.

(a) (b) (c)

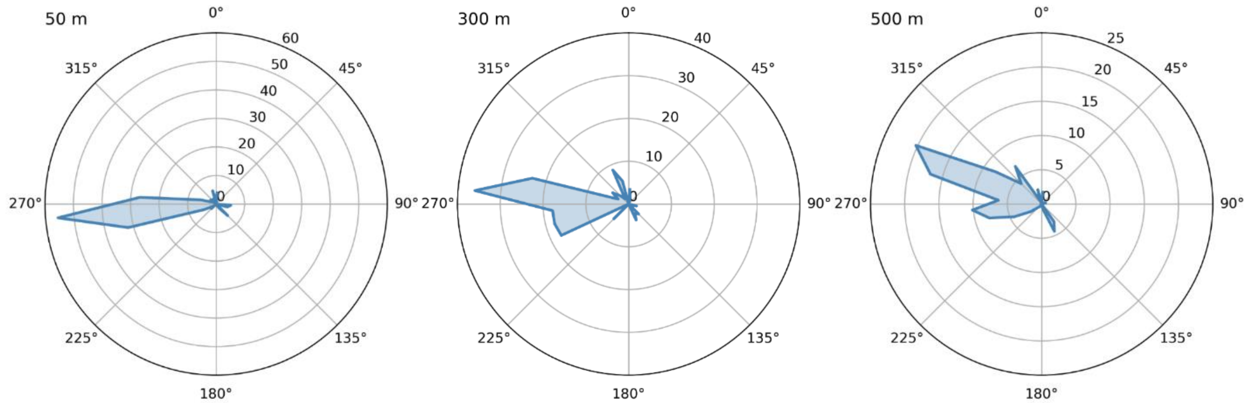

Figure 6. The THF of O_3 through a unit cross-sectional area for various directions at (a) 50 m, (b) 300 m, and (c) 500m AGL during the O_3 pollution episodes in September 2022 (unit: g/m^2).

Table 2. The THF of O_3 through a unit cross-sectional area for six primary groups of directions at 50 m, 300 m, and 500 m AGL during the O_3 pollution episodes in September 2022. The percentage contributions of each component are indicated in parentheses.

Altitudes	THF of O_3 through a unit cross-sectional area (unit: g/m^2)					
	0-60°	60-120°	120-180°	180-240°	240-300°	300-360°
50 m	3.90 (2.4%)	9.22 (5.7%)	7.48 (4.6%)	4.17 (2.6%)	126.33 (78.1%)	10.63 (6.6%)
300 m	4.77 (3.0%)	1.87 (1.2%)	10.16 (6.3%)	5.22 (3.3%)	115.14 (71.9%)	22.96 (14.3%)
500 m	2.08 (2.0%)	0.61 (0.6%)	8.41 (8.3%)	3.10 (3.0%)	65.89 (64.7%)	21.81 (21.4%)

It is worth noting that, as the height increased in the PBL, the peak O_3 flux shifted from westerly (260-270°) at 50 m to northwesterly (290-300°) at 500 m. This rotation can be attributed to the veering wind from the ground to the top of boundary layer. To gain further insights into the vertical variation in the O_3 flux, Figure 7 compares the vertical distribution of the THF of O_3 through a unit cross-sectional area for the directions of (a) 260-270° and (b) 290-300° during the O_3 pollution episodes in September 2022. For the directions between 260° and 270°, the THF of O_3 shows a maximum near the ground, reaching a level of approximately 80 g/m^2 during the O_3 pollution episodes. However, for the directions between 290° and 300°, the THF of O_3 increased with altitude within the PBL, with the total O_3 flux reaching a peak exceeding 20 g/m^2 at 600 m AGL.

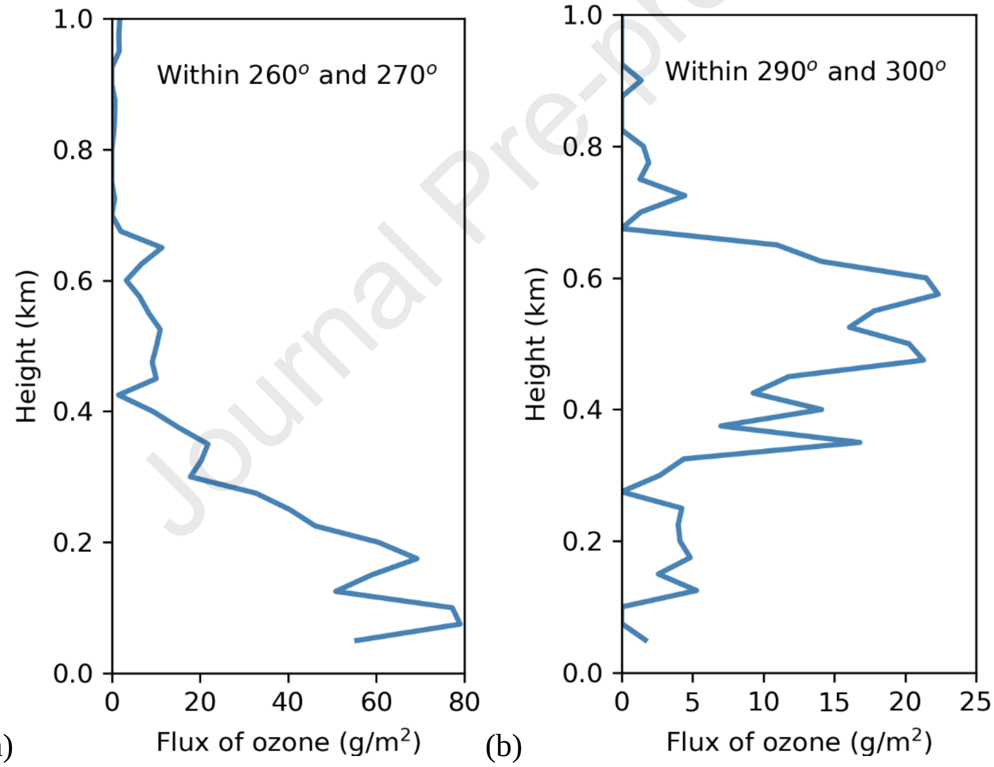

(a) (b)

Figure 7. Vertical distributions of the THF of O_3 through a unit cross-sectional area for the directions of (a) 260-270° and (b) 290-300° during the O_3 pollution episodes in September 2022 (unit: g/m^2).

3.5 O_3 flux across the PBL

In the last section, the THF of O_3 across the entire PBL was analyzed. Panel (a) of Figure 8 shows the THF of O_3 through an area with a width of 1 m across the entire PBL for various directions during the entire study month. For the entire month, the THF of O_3 across the PBL exhibited a predominant easterly component. As summarized in Table 3, the easterly winds between 60° and 120° contributed 49.3% to the total flux of O_3 in the PBL. Panel (b) shows the THF of O_3 through an area with a width of 1 m across the PBL for various directions during the O_3 pollution episodes. During the episodes, the THF of O_3 across the PBL exhibited a predominant westerly component. The westerly winds within 240° and 300° contributed 61.2% to the total flux of O_3 in the PBL. These results indicate that during the pollution episodes, there can be substantial differences in O_3 fluxes compared to the average conditions. These analyses enhanced our understanding of both the short-term variations and long-term average levels of air pollution.

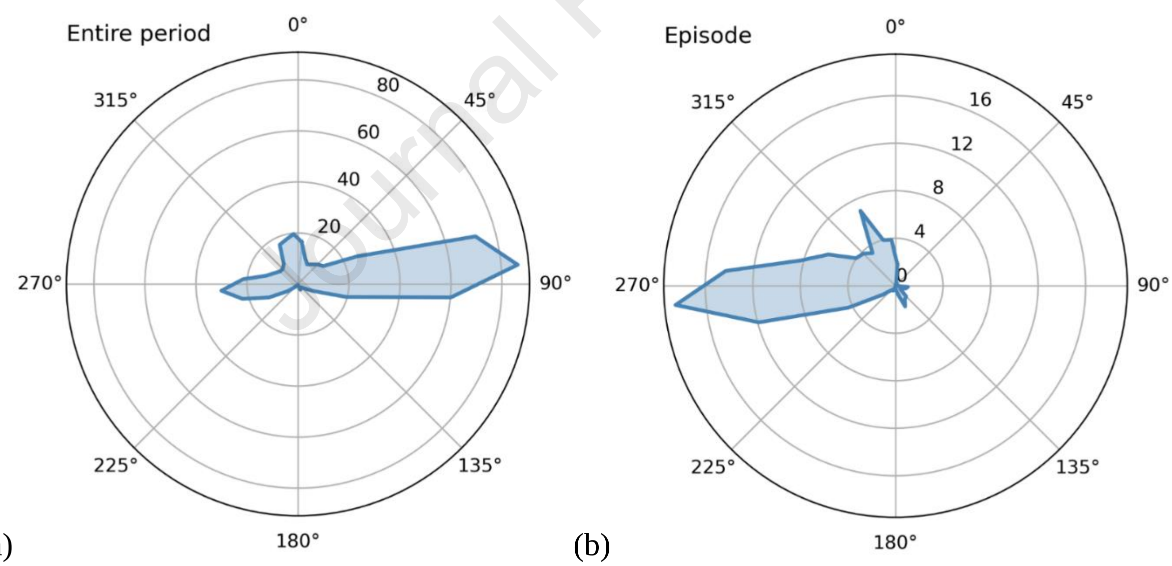

(a) (b)

Figure 8. The THF of O_3 through an area with a width of 1 m across the entire PBL for various directions during (a) the entire study month and (b) O_3 pollution episodes in September 2022 (unit: kg).

Table 3. The THF of O_3 through an area with a width of 1 m across the entire PBL for six primary groups of directions during the entire study month and the O_3 pollution episodes in September

2022. Results for daytime (between 8:00 am and 20:00 pm) and nighttime (before 8:00 am or after 20:00 pm) are also presented. The percentage contributions of each component are indicated in parentheses.

Periods	THF of O_3 across the entire PBL for various directions (unit: kg)						
	0-60°	60-120°	120-180°	180-240°	240-300°	300-360°	All
Entire	68.26 (12.4%)	270.74 (49.3%)	10.65 (1.9%)	8.88 (1.6%)	109.60 (19.9%)	81.31 (14.8%)	549.4
Entire - night	23.71 (9.8%)	149.28 (62.0%)	0.90 (0.38%)	5.78 (2.40%)	34.96 (14.5%)	26.10 (10.8%)	240.7
Entire - day	44.56 (14.4%)	121.47 (39.3%)	9.75 (3.2%)	3.10 (1.0%)	74.64 (24.2%)	55.22 (17.9%)	308.7
Episodes	2.27 (2.2%)	2.94 (2.8%)	6.08 (5.8%)	3.03 (2.9%)	63.64 (61.2%)	26.05 (25.0%)	104.0
Episodes - night	0.03 (0.2%)	1.42 (11.8%)	0.33 (2.8%)	1.32 (11.0%)	8.55 (70.9%)	0.41 (3.4%)	12.1
Episodes - day	2.24 (2.4%)	1.52 (1.7%)	5.74 (6.2%)	1.72 (1.9%)	55.09 (59.9%)	25.64 (27.9%)	91.9

Results for the THF of O_3 in daytime (between 8:00 am and 20:00 pm) and nighttime (before 8:00 am or after 20:00 pm) are also presented in Table 3. Throughout the entire month, the THF of O_3 across the PBL in nighttime was approximately 20% lower than that in daytime. For both the daytime and nighttime throughout the month, the THF of O_3 across the PBL showed a predominant easterly component. During the O_3 episodes, the THF of O_3 across the PBL in daytime was substantially higher than that in the nighttime. These results indicate enhanced photochemical formation during the daytime episodes. For both the daytime and nighttime episodes, the THF of O_3 across the PBL exhibited a predominant westerly component. The westerly winds within 240° and 300° contributed 70.9% and 59.9% to the total flux of O_3 in the PBL for nighttime and daytime, respectively.

Figure 9 shows the daily variation in the THF of O_3 through an area with a width of 1 m across the entire PBL for six primary groups of directions in September 2022. The impacts of the wind from different directions greatly varied. In early September, the northwesterly winds between 300° and 360° played a dominant role in the O_3 transport in Hong Kong. From September 6 to 10, the easterly winds between 60° and 120° governed the O_3 transport. From September 11 to 19, the westerly winds between 240° and 300° played a dominant role in the O_3 transport. After September 20, the O_3 transport was determined by easterly winds between 60° and 120°. As shown in Figure S8, we separated the daily variations in the THF of O_3 across the PBL into nighttime and daytime. For the non-episode periods, the O_3 fluxes in daytime and nighttime were comparable. However, during the O_3 episodes, the O_3 flux greatly increased during the daytime due to enhanced photochemical formation of O_3. These results demonstrate that the source of O_3 transported over Hong Kong varied significantly from day to day. The association between the wind conditions and O_3 transport is apparent.

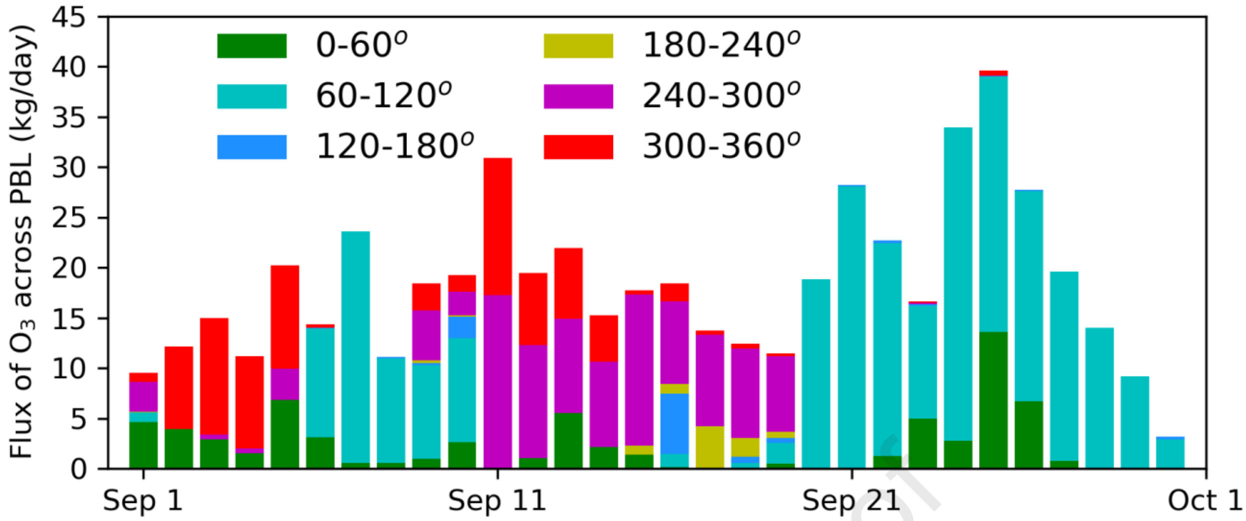

Figure 9. Daily variations in the THF of O_3 through an area with a width of 1 m across the entire PBL for six primary groups of directions in September 2022.

4. Discussion

Ground-level air quality monitoring provides pollutant concentrations at specific locations. However, cross-sectional analyses are necessary to understand pollutant transports across different regions. Analyzing the O_3 flux can help provide answers to questions such as how many pollutants were transported from a specific region (e.g., the central GBA area) into Hong Kong. In the cross-sectional analyses, information on the PBL height is essential because most air pollutants are mixed within the PBL. As a capping inversion layer forms between the PBL and the free atmosphere, we can assume that the interaction between the PBL and the free atmosphere is limited. In this study, cross-sectional analyses were performed at a specific location. However, with more LiDAR systems available at different locations, it is possible to analyze the pollutant flux across the entire boundary between two cities.

This study identified significant impacts of weather systems on O_3 transport. Synoptic patterns featuring a tropical cyclone were found to be conducive to the occurrence of air pollution episodes in Hong Kong. Other synoptic patterns, such as a high pressure system located to the north or a trough located to the south, can significantly increase O_3 concentrations in Hong Kong (Lin et al., 2021). Among these weather patterns, the pollutant flux over Hong Kong can vary significantly. It is worthwhile to extend our study to cover various O_3 episodes under different synoptic patterns over a more extended period. Based on the long-term dataset, the main features of the pollutant transports under different synoptic patterns can be compared.

This study identified significant vertical variance in the wind pattern from the ground up to the top of the PBL. For instance, when the ground-level winds were westerly, the winds at the upper PBL could shift to northwesterly. The veering winds from the bottom to the top of the PBL (i.e., Ekman spiral) can be attributed to the decrease in friction as the altitude increases. In the free atmosphere, friction has a negligible effect, and the wind becomes geostrophic, following the isobars. In the PBL, however, friction causes air to spiral into low-pressure areas. Given the significant vertical variation in the wind pattern, the pollution transports can vary greatly at different altitudes in the PBL. This underscores the importance of using LiDAR techniques to improve our understanding of the 3D transport of air pollutants.

Control of O_3 pollution is a complicated and slow process due to the non-linear response of O_3 to its precursors. Since the implementation of clean air plan in 2013, the O_3 pollution has become a prominent environmental issue in China. Therefore, the transport of O_3 across the GBA and Hong Kong was analyzed in this study. In the GBA and Hong Kong, the annual concentration levels of other pollutants, such as fine particulate matter, are still much higher than the air quality guidelines as recommended by the World Health Organization. Future studies can apply the cross-sectional analyses to understand the transport of other air pollutants, such as particulate matter.

LiDAR measurements provide a unique opportunity to identify the variation in the PBL height. Previous studies have employed various algorithms to estimate the PBL height. In this study, we adopted the method based on the vertical profile of wind speed shear. Reasonable results were obtained, as indicated by the decreased PBL height due to the effect of subsidence at the outer edge of a tropical cyclone. In addition, the PBL height reached its maximum at noontime. These results are consistent with our understanding of the typical variation in the PBL height. This method has some limitations. For example, super-geostrophic phenomena may occur in the nighttime boundary layer (Wang et al., 2023). As a result, wind speeds in the boundary layer can surpass those in the free atmosphere. When the super-geostrophic phenomena occur, our algorithm cannot estimate the PBL height. In such cases, the PBL height will be filled by interpolating adjacent values. In the future, a comprehensive evaluation of the PBL height can be conducted by comparing it with other datasets, such as aerosol LiDAR and meteorological sounding data.

The wind fields in Hong Kong are influenced by complex terrain and architectural features. Firstly, the increased roughness of the urban surface can amplify friction, thereby augmenting the Ekman spiral. Consequently, this can lead to an increased rotation in the wind pattern in relation to altitude. Secondly, the complex architectural features in urban areas increase the thermal contrast between the land and ocean in Hong Kong. Consequently, this enhancement can strengthen the land-sea breeze circulation, which is a ubiquitous mesoscale meteorological phenomenon occurring along the coastal regions of Hong Kong. The complex wind fields, in turn, impact the transport of pollutants in Hong Kong. In this study, wind LiDAR measurements were taken at a single station located in an urban area. The presence of complex wind fields emphasizes the significance of utilizing LiDAR measurements from multiple stations across the territory to track the 3D transport of air pollutants.

Uncertainty in estimating the O_3 flux is determined by several factors, including the PBL height and the vertical profiles of wind and pollutant concentration. Firstly, the PBL height was estimated using wind LiDAR measurements taken on King's Park Hill, which has an elevation of 90 m. The estimation results are slightly lower than those of some other studies, which reported daytime mixing layer heights ranging from 0.6 km to 1.1 km in Hong Kong (Yang et al., 2013). Secondly, uncertainties exist in the wind LiDAR measurements of the upper-level winds. In this study, collocated ground measurements and upper-air radiosonde measurements were used to evaluate the performance of the wind LiDAR. Overall, the wind LiDAR demonstrated a good capability for measuring the vertical profile of wind, exhibiting a mean absolute deviation ranging from 0.5 m/s to 0.7 m/s compared to the collocated measurements (Figure S4). Considering the average wind speeds ranging from approximately 3 m/s to 10 m/s within PBL, the uncertainties arising from the wind measurements remained within 20%.

Vertical variations in pollutant concentrations may exist within the PBL. In this study, we made an assumption that air pollutants are well mixed within the PBL. In a convective mixing layer during the daytime, pollutants can be easily dispersed upward and mixed within the PBL. To gain a deeper understanding of the uncertainty stemming from this assumption, we compare the concentrations of O_3 between Sham Shui Po and Tai Mo Shan. The former is situated at an elevation of 17 meters above sea level, whereas the latter stands at an elevation of 950 meters. As shown in Figure S9, we separate the comparisons into two parts: daytime (between 8:00 am and 20:00 pm) and nighttime (before 8:00 am or after 20:00 pm). Correlation coefficients between O_3 concentrations at the two stations increased from 0.61 for nighttime to 0.87 for daytime, indicating the impacts of enhanced vertical mixing during the daytime. In addition, the mean absolute percentage deviations in the O_3 concentration for the nighttime and daytime were estimated to be 18.9% and 14.0%, respectively. Both of these values fall within the range of 20%. Future analyses can take into account the vertical distribution of pollutant concentrations when the data are available. For instance, the ozone LiDAR system can be used to detect the vertical profile of O_3 concentrations. Synergistic measurements from wind and pollution LiDARs would greatly help to minimize the bias in the estimation of pollution flux in the upper PBL.

5. Conclusion

In this study, measurements from a wind LiDAR system were taken to monitor the vertical profile of wind pattern at an urban site in Hong Kong in September 2022. The PBL height was identified based on the vertical profile of wind speed shear. A cross-sectional analysis was performed to explore the THF of O_3 across the PBL in Hong Kong. Clockwise veering winds were observed from the ground to the top of the PBL, which can be attributed to the decreased influence of friction with increasing height. As a result, the wind with the peak O_3 flux shifted from westerly to northwesterly as the height increased in the PBL. Throughout the study month, the THF of O_3 exhibited a predominant easterly component. However, during the O_3 pollution episodes, the THF of O_3 exhibited a predominant westerly component, indicating an increased regional transport of pollutants from the GBA. These analyses provide insights into both the short-term variations and long-term average levels of air pollution. The findings enhance our understanding of the 3D pollutant transports in the GBA and Hong Kong. Future studies can combine wind and pollution LiDAR to minimize the bias in the estimation of pollution flux in the upper PBL.

Supplement

Additional figures (Figures S1–S9).

Competing interests

The authors declare that they have no actual or potential competing financial interests.

Acknowledgments

This work was supported by the RGC - Collaborative Research Fund (Grant No. C6026-22GF), the NSFC/RGC Joint Research Project (Grant Nos. N_HKUST638/19 and N_HKUST609/21), CUHK: Research Sustainability of Major RGC Funding Schemes 18-19 (CRF-16/17-C4020-16G-3133195), and the Research Grants Council of Hong Kong (Project No. T24/504/17). We thank HKUST Institute for the Environment and Environmental Central Facility (http://envf.ust.hk/dataview) for providing meteorological and air quality data.

Reference

Canut, G., Couvreux, F., Lothon, M., Pino, D., Saïd, F., 2012. Observations and Large-Eddy Simulations of Entrainment in the Sheared Sahelian Boundary Layer. Boundary-Layer Meteorol 142, 79–101. https://doi.org/10.1007/s10546-011-9661-x

Chen, T., Fu, J.Y., Chan, P.W., He, Y.C., Liu, A.M., Zhou, W., 2023. Wind characteristics in typhoon boundary layer at coastal areas observed via a Lidar profiler. Journal of Wind Engineering and Industrial Aerodynamics 232, 105253. https://doi.org/10.1016/j.jweia.2022.105253

Cruz, M.T., Simpas, J.B., Sorooshian, A., Betito, G., Cambaliza, M.O.L., Collado, J.T., Eloranta, E.W., Holz, R., Topacio, X.G.V., Del Socorro, J., Bagtasa, G., 2023. Impacts of regional wind circulations on aerosol pollution and planetary boundary layer structure in Metro Manila, Philippines. Atmospheric Environment 293, 119455. https://doi.org/10.1016/j.atmosenv.2022.119455

Ekman, V.W., Kullenberg, B., 1905. On the influence of the earth's rotation on ocean-currents. Ark. Mat. Astron 2, 1–53.

Fan, S., Li, Y., 2023. Potential deterioration of ozone pollution in coastal areas caused by marine-emitted halogens: A case study in the Guangdong-Hong Kong-Macao Greater Bay Area. Science of The Total Environment 860, 160456. https://doi.org/10.1016/j.scitotenv.2022.160456

Fung, J.C.H., Lau, A.K.H., Lam, J.S.L., Yuan, Z., 2005. Observational and modeling analysis of a severe air pollution episode in western Hong Kong. Journal of Geophysical Research: Atmospheres 110. https://doi.org/10.1029/2004JD005105

Guo, J., Zhang, X., Gao, Y., Wang, Zhangwei, Zhang, M., Xue, W., Herrmann, H., Brasseur, G.P., Wang, T., Wang, Zhe, 2023. Evolution of Ozone Pollution in China: What Track Will It Follow? Environ. Sci. Technol. 57, 109–117. https://doi.org/10.1021/acs.est.2c08205

He, Y., Ren, C., Mak, H.W.L., Lin, C., Wang, Z., Fung, J.C.H., Li, Y., Lau, A.K.H., Ng, E., 2021. Investigations of high-density urban boundary layer under summer prevailing wind conditions with Doppler LiDAR: A case study in Hong Kong. Urban Climate 38, 100884. https://doi.org/10.1016/j.uclim.2021.100884

Jiang, Y., Li, B., He, H., Li, X., Wang, D., Peng, Z., 2022. Identification of the atmospheric boundary layer structure through vertical distribution of PM2.5 obtained by unmanned aerial vehicle measurements. Atmospheric Environment 278, 119084. https://doi.org/10.1016/j.atmosenv.2022.119084

Li, L., Lu, C., Chan, P.-W., Lan, Z., Zhang, W., Yang, H., Wang, H., 2022. Impact of the COVID-19 on the vertical distributions of major pollutants from a tower in the Pearl River Delta. Atmospheric Environment 276, 119068. https://doi.org/10.1016/j.atmosenv.2022.119068

Li, Y., Lau, A.K.H., Fung, J.C.H., Ma, H., Tse, Y., 2013. Systematic evaluation of ozone control policies using an Ozone Source Apportionment method. Atmospheric Environment, Improving Regional Air Quality over the Pearl River Delta and Hong Kong: from Science to Policy 76, 136–146. https://doi.org/10.1016/j.atmosenv.2013.02.033

Lin, C., Leung, K.K.M., Yu, A.L.C., Tsang, R.C.W., Tsui, W.B.C., Fung, J.C.H., Ng, E.K.W., Cheung, S.L., Tang, A.W.Y., Ning, Z., Li, Y., Zhang, T., Lau, A.K.H., 2021. Effects of synoptic patterns on the vertical structure of ozone in Hong Kong using lidar measurement. Atmospheric Environment 257, 118490. https://doi.org/10.1016/j.atmosenv.2021.118490

Lindvall, J., Svensson, G., 2019. Wind turning in the atmospheric boundary layer over land. Quarterly Journal of the Royal Meteorological Society 145, 3074–3088. https://doi.org/10.1002/qj.3605

Liu, B., Ma, X., Ma, Y., Li, H., Jin, S., Fan, R., Gong, W., 2022. The relationship between atmospheric boundary layer and temperature inversion layer and their aerosol capture capabilities. Atmospheric Research 271, 106121. https://doi.org/10.1016/j.atmosres.2022.106121

Park, S., Kim, M.-H., Yeo, H., Shim, K., Lee, H.-J., Kim, C.-H., Song, C.-K., Park, M.-S., Shimizu, A., Nishizawa, T., Kim, S.-W., 2022. Determination of mixing layer height from co-located lidar, ceilometer and wind Doppler lidar measurements: Intercomparison and implications for PM2.5 simulations. Atmospheric Pollution Research 13, 101310. https://doi.org/10.1016/j.apr.2021.101310

Paul, B., Das, A.K., 2022. Spatial heterogeneity in boundary layer dynamism and PM2.5 surface concentration over the complex terrain of Brahmaputra valley. Remote Sensing Applications: Society and Environment 28, 100828. https://doi.org/10.1016/j.rsase.2022.100828

Potts, D.A., Timmis, R., Ferranti, E.J.S., Vande Hey, J.D., 2023. Identifying and accounting for the Coriolis effect in satellite NO_2 observations and emission estimates. Atmospheric Chemistry and Physics 23, 4577–4593. https://doi.org/10.5194/acp-23-4577-2023

Shen, L., Liu, J., Zhao, T., Xu, X., Han, H., Wang, H., Shu, Z., 2022. Atmospheric transport drives regional interactions of ozone pollution in China. Science of The Total Environment 830, 154634. https://doi.org/10.1016/j.scitotenv.2022.154634

Su, T., Li, Z., Zheng, Y., Luan, Q., Guo, J., 2020. Abnormally Shallow Boundary Layer Associated With Severe Air Pollution During the COVID-19 Lockdown in China. Geophysical Research Letters 47, e2020GL090041. https://doi.org/10.1029/2020GL090041

Tang, K., Zhang, H., Feng, W., Liao, H., Hu, J., Li, N., 2022. Increasing but Variable Trend of Surface Ozone in the Yangtze River Delta Region of China. Frontiers in Environmental Science 10.

Tse, K.T., Weerasuriya, A.U., Kwok, K.C.S., 2016. Simulation of twisted wind flows in a boundary layer wind tunnel for pedestrian-level wind tunnel tests. Journal of Wind

Engineering and Industrial Aerodynamics 159, 99–109. https://doi.org/10.1016/j.jweia.2016.10.010

Tucker, S.C., Senff, C.J., Weickmann, A.M., Brewer, W.A., Banta, R.M., Sandberg, S.P., Law, D.C., Hardesty, R.M., 2009. Doppler Lidar Estimation of Mixing Height Using Turbulence, Shear, and Aerosol Profiles. Journal of Atmospheric and Oceanic Technology 26, 673–688. https://doi.org/10.1175/2008JTECHA1157.1

Wang, L., Liu, J., Gao, Z., Li, Y., Huang, M., Fan, S., Zhang, X., Yang, Y., Miao, S., Zou, H., Sun, Y., Chen, Y., Yang, T., 2019. Vertical observations of the atmospheric boundary layer structure over Beijing urban area during air pollution episodes. Atmospheric Chemistry and Physics 19, 6949–6967. https://doi.org/10.5194/acp-19-6949-2019

Wang, S., Guo, J., Xian, T., Li, N., Meng, D., Li, H., Cheng, W., 2023. Investigation of low-level supergeostrophic wind and Ekman spiral as observed by a radar wind profiler in Beijing. Frontiers in Environmental Science 11.

Xia, D., Sun, L., Wang, J., Nie, H., Chow, K.-C., Chan, K.L., Wang, D., Jiang, C., 2023. Correspondence between urbanization and surface wind in the Guangdong-Hong Kong-Macao Greater Bay Area: Observations and idealized large-eddy simulation. Urban Climate 49, 101475. https://doi.org/10.1016/j.uclim.2023.101475

Yan, Y., Cai, X., Miao, Y., Yu, M., 2022. Synoptic condition and boundary layer structure regulate PM2.5 pollution in the Huaihe River Basin, China. Atmospheric Research 269, 106041. https://doi.org/10.1016/j.atmosres.2022.106041

Yang, D., Li, C., Lau, A.K.-H., Li, Y., 2013. Long-term measurement of daytime atmospheric mixing layer height over Hong Kong. Journal of Geophysical Research: Atmospheres 118, 2422–2433. https://doi.org/10.1002/jgrd.50251

Yang, S.-C., Cheng, F.-Y., Wang, L.-J., Wang, S.-H., Hsu, C.-H., 2022. Impact of lidar data assimilation on planetary boundary layer wind and PM2.5 prediction in Taiwan. Atmospheric Environment 277, 119064. https://doi.org/10.1016/j.atmosenv.2022.119064

Yang, Y., Yim, S.H.L., Haywood, J., Osborne, M., Chan, J.C.S., Zeng, Z., Cheng, J.C.H., 2019. Characteristics of Heavy Particulate Matter Pollution Events Over Hong Kong and Their Relationships With Vertical Wind Profiles Using High-Time-Resolution Doppler Lidar Measurements. Journal of Geophysical Research: Atmospheres 124, 9609–9623. https://doi.org/10.1029/2019JD031140

Yu, Z., Xiao, Z., Liu, X., 2023. Characterizing the spatial-functional network of regional industrial agglomerations: A data-driven case study in China's greater bay area. Applied Geography 152, 102901. https://doi.org/10.1016/j.apgeog.2023.102901

Zhang, C., Wang, Q., Chan, P.W., Li, Y., 2023. Performance of summertime temperature and wind fields under different background winds in Kowloon, Hong Kong. Urban Climate 49, 101444. https://doi.org/10.1016/j.uclim.2023.101444

Zhang, S., Li, B., Solari, G., Zhang, X., Xu, X., 2021. A Refined Study of Atmospheric Wind Properties in the Beijing Urban Area Based on a 325 m Meteorological Tower. Atmosphere 12, 786. https://doi.org/10.3390/atmos12060786

Zhou, X., Ren, J., Gui, C., An, J., Xiao, C., Tao, Y., Shi, X., Jin, X., Yan, D., 2022. Generation and verification of vertical meteorological data for building energy simulation from a 325-meter Beijing meteorological tower. Energy and Buildings 262, 111992. https://doi.org/10.1016/j.enbuild.2022.111992

Highlights

- Total horizontal flux (THF) of O_3 across the PBL was explored using a wind LiDAR
- The PBL height was identified based on the vertical profile of wind speed shear
- The THF of O_3 exhibited a predominant westerly component during O_3 episodes
- Clockwise veering flux of O_3 were observed from the ground to the top of the PBL
- Our results enhance our understanding of the 3D pollutant transports in the GBA

Declaration of interests

☒ The authors declare that they have no known competing financial interests or personal relationships that could have appeared to influence the work reported in this paper.

☐ The authors declare the following financial interests/personal relationships which may be considered as potential competing interests: